J|A|C|S
ARTICLES
Published on Web 10/04/2002

Ordered Nanoporous Polymers from Polystyrene−Polylactide Block Copolymers

Andrew S. Zalusky, Roberto Olayo-Valles,† Johanna H. Wolf, and Marc A. Hillmyer*

Contribution from the Department of Chemistry, University of Minnesota, 207 Pleasant Street SE, Minneapolis, Minnesota 55455-0431

Received July 25, 2002

Abstract: Nanoporous polystyrene monoliths were prepared from polystyrene−polylactide (**PS**−**PLA**) block copolymers that form hexagonally packed nanocylinders of **PLA** in a **PS** matrix. A morphology diagram was developed to determine the range in composition and molecular weight over which this morphology existed. Macroscopic alignment of these materials gave anisotropic monoliths that were subjected to mild degradation conditions leading to the chemical etching of the **PLA**. The resulting nanoporous monoliths consisted of a polystyrene matrix containing hexagonally close-packed, oriented, and continuous nanoscopic channels (pore size was tunable through synthesis or blending) lined with chemically accessible hydroxyl functional groups. Both the precursors and the porous materials were analyzed moleculary (size-exclusion chromatography and proton nuclear magnetic resonance spectroscopy) and structurally (small-angle X-ray scattering, scanning electron microscopy, and differential scanning calorimetry). In addition, the surface area and pore size distribution of the nanoporous monoliths were characterized (N_2 adsorption measurements). These nanoporous materials have remarkable potential as hosts for nanomaterial synthesis, size-selective catalyst supports, and advanced separations.

Introduction

Block copolymers are fascinating and complex soft materials that have been used in diverse scientific and technological capacities. While block copolymers are found in everyday items such as box tape and asphalt,[1] they have also been employed to understand interesting and broadly important physical phenomena in ordered soft materials.[2] Predictable self-assembly and the wide array of accessible block structures have further enabled scientific and technologically relevant advances using these hybrid materials. Examples of technologically relevant applications include the preparation of interesting materials such as semiconductor nanoparticles,[3−5] robust vesicles,[6] polymeric electrolytes,[7,8] mechanically tough nanocomposites,[9−11] and nanoporous polymers.[12] With respect to the latter materials, block copolymers are arguably ideal precursors for the formation of ordered nanoporous organic polymers.

Nanoporous polymers can be prepared by several routes including controlled foaming,[13,14] ion track etching,[15] and molecular imprinting.[16] These materials are important due to their potential and established utility as separation media,[17] interlayer dielectrics,[18−20] catalysts,[21,22] and templates for the growth of nanoscopic materials.[23] The preparation of ordered nanoporous polymers from block copolymer precursors was established in 1988 by Nakahama.[24] In that work, a siloxane-functionalized polystyrene (**PS**) was incorporated into a block copolymer with polyisoprene as the minority component. The resultant material formed a hexagonally packed array of polyisoprene cylinders in the functionalized **PS** matrix. Upon cross-linking a thin film of this block copolymer through the

* To whom correspondence should be addressed. E-mail: hillmyer@chem.umn.edu.

† Department of Chemical Engineering and Materials Science, University of Minnesota.

(1) Holden, G.; Legge, N. R.; Quirk, R.; Schroeder, H. E. *Thermoplastic Elastomers*, 2nd ed.; Schoder Druck GmbH & Co KG: Gersthofen, 1996.
(2) Hamley, I. W. *The Physics of Block Copolymers*; Oxford University Press: Oxford, 1998.
(3) Fogg, D. E.; Radzilowski, L. H.; Balnski, R.; Schrock, R. R.; Thomas, E. L. *Macromolecules* **1997**, *30*, 417−426.
(4) Chan, Y. N. C.; Schrock, R. R.; Cohen, R. E. *Chem. Mater.* **1992**, *4*, 24−27.
(5) Förster, S.; Antonietti, M. *Adv. Mater.* **1998**, *10*, 195−217.
(6) Discher, B. M.; Bermudez, H.; Hammer, D. A.; Discher, D. E.; Won, Y.-Y.; Bates, F. S. *J. Phys. Chem. B* **2002**, *106*, 2848−2854.
(7) Ruzette, A.-V. G.; Soo, P. P.; Sadoway, D. R.; Mayes, A. M. *J. Electrochem. Soc.* **2001**, *148*, A537−A543.
(8) Matsumi, N.; Sugai, K.; Ohno, H. *Macromolecules* **2002**, *35*, 5731−5733.
(9) Hillmyer, M. A.; Lipic, P. M.; Hajduk, D. A.; Almdal, K.; Bates, F. S. *J. Am. Chem. Soc.* **1997**, *119*, 2749−2750.
(10) Lipic, P. M.; Bates, F. S.; Hillmyer, M. A. *J. Am. Chem. Soc.* **1998**, *120*, 8963−8970.
(11) Dean, J. M.; Lipic, P. M.; Grubbs, R. B.; Cook, R. F.; Bates, F. S. *J. Polym. Sci., Part B: Polym. Phys.* **2001**, *39*, 2996−3010.
(12) Buchmeiser, M. R. *Angew. Chem., Int. Ed.* **2001**, *40*, 3795−3797.
(13) Krause, B.; Sijbesma, H. J. P.; Münüklü, P.; van der Vegt, N. F. A.; Wessling, M. *Macromolecules* **2001**, *34*, 8792−8801.
(14) Krause, B.; Diekmann, K.; van der Vegt, N. F. A.; Wessling, M. *Macromolecules* **2002**, *35*, 1738−1745.
(15) Martin, C. R. *Chem. Mater.* **1996**, *8*, 1739−1746.
(16) Wulff, G. *Chem. Rev.* **2002**, *102*, 1−28.
(17) Miroslav, J.; Sykora, D.; Svec, F.; Frechet, J. M. J.; Schweer, J.; Holm, R. *J. Polym. Sci., Part A: Polym. Chem.* **2000**, *38*, 2767−2778.
(18) Nguyen, C. V.; Carter, K. R.; Hawker, C. J.; Hedrick, J. L.; Jaffe, R. L.; Miller, R. D.; Remenar, J. F.; Rhee, H.-W.; Rice, P. M.; Toney, M. F.; Trollsås, M.; Yoon, D. Y. *Chem. Mater.* **1999**, *11*, 3080−3085.
(19) Hedrick, J. L.; Hawker, C. J.; DiPietro, R.; Jerome, R.; Charlier, Y. *Polymer* **1995**, *36*, 4855−4866.
(20) Hedrick, J. L.; Miller, R. D.; Hawker, C. J.; Carter, K. R.; Volksen, W.; Yoon, D. Y.; Trollsås, M. *Adv. Mater.* **1998**, *10*, 1049−1053.
(21) Deng, H.; Gin, D. L.; Smith, R. C. *J. Am. Chem. Soc.* **1998**, *120*, 3522−3523.
(22) Gu, W.; Zhou, W.-J.; Gin, D. L. *Chem. Mater.* **2001**, *13*, 1949−1951.
(23) Martin, C. R. *Science* **1994**, *266*, 1961−1966.
(24) Lee, J.; Hirao, A.; Nakahama, S. *Macromolecules* **1988**, *21*, 274−276.

siloxane moieties and subjecting the film to ozonolysis to remove the polyisoprene, a cross-linked material was obtained with nanopores templated by the block copolymer precursor. Following this work, Hashimoto, Hedrick, Liu, Russell, Thomas, and others have employed related strategies to achieve ordered and disordered nanoporous polymers.[25−36]

As is evident from these examples, the use of model block copolymers with reactive functionalities has been particularly important. In addition, most of the block copolymer precursor routes to ordered nanoporous materials have several other features in common. First, these preparative protocols are generally restricted to thin films ($<10\ \mu$m). Second, the matrix of the nanoporous material is a cross-linked polymer. Third, the identity and accessibility of the functionality in the pore wall has generally not been established or is difficult to control. While these features have not limited the success of these nanoporous materials in applications as diverse as selective membranes to nanowire templates, a flexible and tunable strategy for the formation of ordered nanoporous polymers of any shape or size, with predictable and accessible wall functionality, amenable to solvent or low temperature processing, and with tunable pore sizes and topologies is desirable. In this regard, we recently communicated a robust synthetic methodology for the formation of ordered **PS** monoliths with controlled nanoporosity.[37]

The methodology we employed required the synthesis of polystyrene-polylactide (**PS−PLA**) block copolymers by a combination of polymerization mechanisms. In our preliminary account we described a material that formed cylinders (22 nm in diameter) of **PLA** hexagonally packed in a **PS** matrix with an intercylinder (center-to-center) spacing of 34 nm. Macroscopic alignment of these cylinders using reciprocating shear followed by degradation in aqueous base led to a bulk sample of nanoporous polystyrene. We characterized this nanoporous material using small-angle X-ray scattering (SAXS) and scanning electron microscopy (SEM) to confirm both the porosity and long-range order of the sample. This proof of principle example provided the impetus to explore the generality and flexibility of this approach to ordered nanoporous materials. Furthermore, we wished to fully characterize the porous materials in terms of their internal surface area, thermal stability, and pore wall functionality.

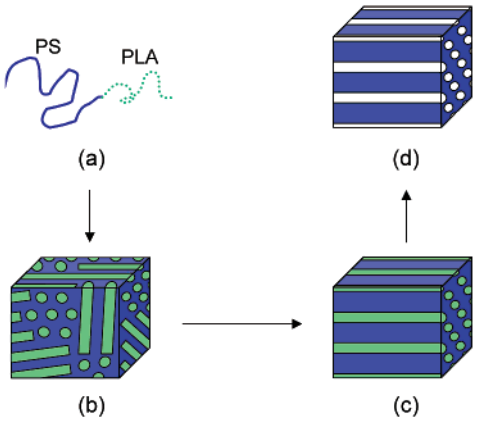

Figure 1. Pathway to nanoporous materials: (a) **PS−PLA** diblock copolymer. (b) Self-assembled-polydomained cylindrical morphology. (c) Shear-aligned monolith. (d) Nanoporous monolith obtained through the hydrolytic removal of **PLA**.

In this manuscript we provide the results of a complete examination of the **PS−PLA** block copolymer system as a reactive block copolymer template for the formation of ordered nanoporous organic polymers. An overview of our protocol is shown in Figure 1. We first report the detailed synthesis, self-assembly, and microstructural alignment of the precursor **PS−PLA** materials. Focusing on the cylindrical morphology, we describe the degradation of the **PLA** component followed by a complete characterization of the ordered nanoporous materials including N_2 adsorption, differential scanning calorimetry (DSC), SEM, and SAXS. The key features of this system for the formation of ordered nanoporous polymers are provided and include a morphology map for **PS−PLA** block copolymers, the demonstration of tunable pore sizes, high degrees of pore alignment with simple techniques, estimates of pore fidelity (i.e., defect identity), thermal stability of the porous monoliths, and the accessibility of the pore wall functionality.

Experimental Section

General Methods. All ^{1}H NMR spectra were recorded on a Varian 300 VXR spectrometer. The NMR samples were prepared in deuterated chloroform (Cambridge) at concentrations of roughly 1 wt %. The IR spectra were collected on a Nicolet Magna-IR Spectrometer 550. IR samples were prepared by crushing the sample and dried KBr (in 1:10 ratio by volume) with mortar and pestle and then pressing the mixture into a pellet using a screw-press. All size-exclusion chromatography (SEC) data were obtained using a Hewlett-Packard 1100 series liquid chromatograph equipped with Jordi polydivinylbenzene columns with pore sizes of 10000, 1000, and 500 Å as well as a Hewlett-Packard 1047A refractive index detector. Tetrahydrofuran at 35 °C with a flow rate of 1 mL/min was used as the mobile phase. The instrument was calibrated with polystyrene standards (Polymer Laboratories). All differential scanning calorimetry (DSC) analyses were performed on a Perkin-Elmer DSC-7. An indium standard was used to calibrate the instrument and nitrogen was used as the purge gas. The scan rate used for the samples was 10 °C/min.

Materials. All reagents and solvents were used as received unless otherwise noted. Styrene (Aldrich) was purified by stirring over CaH_2 (Aldrich) for about 16 h followed by distillation into a flask containing dibutylmagnesium obtained through removal of the solvent under reduced pressure from 5 mL of a 1.0 M heptane solution of dibutylmagnesium (Aldrich). This was stirred for about 2 h before the styrene was transferred to a flame-dried buret. Ethylene oxide (Aldrich) was purified in the same manner as styrene. The concentration of *sec*-butyllithium (Aldrich) was determined using the Gillman double titration

(25) Mecerreyes, D.; Huang, E.; Magbitang, T.; Volksen, W.; Hawker, C. J.; Lee, V. Y.; Miller, R. D.; Hedrick, J. L. *High Perform. Polym.* **2001**, *13*, S11−S19.
(26) Liu, G.; Hu, N.; Xu, X.; Yao, H. *Macromolecules* **1994**, *27*, 3892−3895.
(27) Liu, G.; Ding, J.; Guo, A.; Herfort, M.; Bazzett-Jones, D. *Macromolecules* **1997**, *30*, 1851−1853.
(28) Liu, G. *Curr. Opin. Colloid Interface Sci.* **1998**, *3*, 200−208.
(29) Liu, G.; Ding, J.; Hashimoto, T.; Kimishima, K.; Winnik, F.; Nigam, S. *Chem. Mater.* **1999**, *11*, 2233−2240.
(30) Hashimoto, T.; Tsutsumi, K.; Funaki, Y. *Langmuir* **1997**, *13*, 6869−6872.
(31) Thurn-Albrecht, T.; Schotter, J.; Kästle, G. A.; Emley, N.; Shibauchi, T.; Krusin-Elbaum, L.; Guarini, K.; Black, C. T.; Tuominen, M. T.; Russell, T. P. *Science* **2000**, *290*, 2126−2129.
(32) Thurn-Albrecht, T.; Steiner, R.; DeRouchey, J.; Stafford, C. M.; Huang, E.; Bal, M.; Trouminen, M.; Hawker, C. J.; Russell, T. P. *Adv. Mater.* **2000**, *12*, 787−791.
(33) Xu, T.; Kim, H.-C.; DeRouchey, J.; Seney, C.; Levesque, C.; Martin, P.; Stafford, C. M.; Russell, T. P. *Polymer* **2001**, *42*, 9091−9095.
(34) Avgeropoulos, A.; Chan, V. Z.-H.; Lee, V. Y.; Ngo, D.; Miller, R. D.; Hadjichristidis, N.; Thomas, E. L. *Chem. Mater.* **1998**, *10*, 2109−2115.
(35) Chan, V. Z.-H.; Hoffman, J.; Lee, V.; Latrou, H.; Avgeropoulos, A.; Hadjichristidis, N.; Miller, R. D.; Thomas, E. L. *Science* **1999**, *286*, 1716−1719.
(36) Park, M.; Harrison, C.; Chaikin, P. M.; Register, R. A.; Adamson, D. H. *Science* **1997**, *276*, 1401−1404.
(37) Zalusky, A. S.; Olayo-Valles, R.; Taylor, C. J.; Hillmyer, M. A. *J. Am. Chem. Soc.* **2001**, *123*, 1519−1520.

Table 1. Characterization of **PSOH** Samples

sample[a]	M_n (kg/mol)[b]	N[c]	M_n (kg/mol)[d]	M_w/M_n[d]	[OH]/[*s*-Bu][e]
PSOH(5)	4.9	43	4.1	1.04	1.01
PSOH(8)	8.0	70	6.1	1.04	1.00
PSOH(9)	9.0	79	8.9	1.02	0.99
PSOH(18)	18	156	15	1.02	0.99
PSOH(22)	22	192	18	1.02	1.03
PSOH(34)	34	295	31	1.04	1.02
PSOH(56)	56	491	48	1.05	1.07

[a] **PSOH(*X*)** = hydroxyl-terminated polystyrene with a total molecular weight (***X*** kg/mol). [b] **PSOH** molecular weights were determined from ^{1}H NMR end group analysis and agree with the expected molecular weight from stoichiometry. [c] Degree of polymerization calculated from molecular weight, density at 110 °C (ρ_{PS} = 1.02 g/cm^3 and ρ_{PLA} = 1.18 g/cm^3) and a reference volume of 185 Å^3.[102,103] [d] SEC versus polystyrene standards. [e] The end group ratio for **PSOH** was determined through ^{1}H NMR analysis. [OH]/[*s*-Bu] is the molar ratio of the methylene (adjacent to the hydroxyl group) resonance of the ethoxy end group to that of the methyl resonances of the *s*-butyl initiator.

method.[38] D,L-lactide (Aldrich) was purified by recrystallization from ethyl acetate and then dried under reduced pressure at room temperature. ^{1}H NMR spectroscopy was used to confirm its purity, and the purified D,L-lactide was then stored under argon in a drybox. Degassed cyclohexane and toluene were purified by passage through an activated alumina column to remove protic impurities followed by passage through a supported copper catalyst to remove oxygen using a home-built purification line described previously.[39] The solvents were collected in flame-dried air-free flasks.

Synthesis of Hydroxyl-terminated Polystyrene (PSOH). We employed an approach to **PSOH** similar to a previously reported method for the synthesis of hydroxyl-terminated polyisoprene.[39] An example of one such polymerization is described (**PSOH(22)** in Table 1 where **PSOH(*X*)** = hydroxyl-terminated **PS** with a total molecular weight (***X*** kg/mol)). The polymerization was performed in a 2-L flask containing a Teflon-coated magnetic stir bar. The flask was fitted with five threaded glass connectors; three were fitted with glass plugs using Ace Glass bushings and FETFE O-rings, one was plugged with a thermowell, and the last was fitted with a Y-connector. The Y-connector had three ports. Two of the ports were fitted with Teflon valves from which one interfaced the argon/vacuum manifold, while the other interfaced the manometer. The third port was plugged with a septum. The reactor was evacuated to nearly 10^{-3} Torr and baked for 16 h at 275 °C. Once the reactor was cooled to room temperature, the three glass plugs were replaced, under a positive pressure of argon, by a buret of purified styrene (98.7 g, 0.949 mol), a buret of purified ethylene oxide (10.0 g, 0.227 mol), and a flask containing 0.7 L of purified cyclohexane. The burets of styrene and cyclohexane were connected directly to the reaction vessel, whereas the buret of ethylene oxide was connected to the vessel via a flexible Cajon Ultratorr fitting. This allowed for the ethylene oxide to be immersed in an ice bath, thus keeping the pressure in the buret low. The reactor was evacuated and backfilled with argon six times. The pressure of the reaction vessel was monitored to ensure that no leaks were present in the system. The cyclohexane was then added to the reaction vessel. This was followed by the addition of the initiator, *sec*-butyllithium (3.82 mL of 1.29 M *sec*-butyllithium/cyclohexane solution, 4.93×10^{-3} mol) through the septum using a syringe (the *sec*-butyllithium solution was kept in the drybox until needed). The styrene was then added to the cyclohexane/initiator mixture at a steady rate. The reaction mixture was heated using a 43 °C water bath. The reaction mixture became an orange-red color. Within 10 min of initiation, the reaction mixture reached a temperature of 53 °C, accompanied by an increase in the pressure. The reaction mixture cooled to 42 °C and was allowed to stir for 4.3 h. The reaction mixture was cooled to room temperature before the ethylene oxide was added. Upon the addition of the ethylene oxide, the reaction mixture immediately became colorless. This mixture was stirred at room temperature for 14 h and then vented under a positive argon pressure. The product was precipitated into a 50:50 (by volume) mixture of 2-propanol and methanol at room temperature. A white precipitate was collected by vacuum filtration and dried at 112 °C under vacuum for 15 h. The yield was 94.2 g (95.4%). M_n of this representative **PSOH** was 21.8 kg/mol by ^{1}H NMR end group analysis and 19.1 kg/mol by SEC analysis which were close to the targeted molecular weight of 20 kg/mol. SEC analysis gave a M_w/M_n of 1.02.

Synthesis of Polystyrene−Polylactide (PS−PLA). All lactide polymerizations were assembled and capped in the drybox and performed in dry toluene with [lactide]$_0$ = 1.0 M. Equal molar amounts of both triethylaluminum (Et_3Al) and **PSOH** were used to form an aluminum alkoxide macroinitiator. The synthesized diblocks were precipitated in methanol and collected by vacuum filtration. The block copolymers were then dried under vacuum at temperatures ranging from 100 to 120 °C. A sample synthesis of **PS−PLA** is given hereafter (**SL(37, 0.38)** in Table 2 where **SL(*X*,*Y*)** = **PS−PLA** with total molecular weight (***X*** kg/mol**)** and **PLA** volume fraction (***Y***)). A 48 mL high-pressure flask was silanized by applying a 10/90 (by volume) solution of dichlorodimethylsilane/methylene chloride to the flask and then drying it at 120 °C for 1 h. In a drybox, to the silanized flask was added 3.0 g of **PSOH(22)** in Table 1 (1.38×10^{-4} mol), 24 mL of dry toluene and 75 μL of a 1.9 M Et_3Al in toluene solution (1.42×10^{-4} mol) by syringe. This was stirred for 12 h to allow for macroinitiator formation. D,L-lactide (3.84 g, 0.0242 mol) was added to the flask. The reaction vessel was capped and removed from the drybox. It was then immersed in an 80 °C oil bath and stirred for 26 h after which the reaction was terminated with acidic methanol and precipitated in methanol. The block copolymer was collected by vacuum filtration and then dried under vacuum at 110 °C for 16 h. The conversion of lactide in the polymerization was 60% based on isolation yield assuming complete recovery of **PS** which agreed with that determined from ^{1}H NMR spectroscopy. The block copolymer was characterized by SEC (M_w/M_n = 1.10) and ^{1}H NMR spectroscopy (M_n = 37.0 kg/mol).

^{1}H NMR and IR Characterization of PSOH and PS−PLA. The following ^{1}H NMR resonances are representative of the polymeric samples contained in this paper. All ^{1}H NMR resonances are reported in ppm downfield from tetramethylsilane (0.0 ppm). The signals were either broad (b) or resulted from multiple resonances (m). **PSOH**: 6.8 (m, aromatic protons), 3.3 (b, PS−CH_2−C**H$_2$**−OH), 1.7 (m, −C**H**(C_6H_5)−C**H$_2$**−), 0.9 (b, −C**H$_2$**− of initiator), 0.7 (m, −C**H$_3$** of initiator). **PS−PLA**: The **PS** resonances are the same as given above except that the diblocks have a (b, PS−CH_2−C**H$_2$**−O−PLA) resonance at 3.8 ppm. **PLA** resonances are: 5.2 (m, −C(O)−C**H**(CH_3)−O−) and 1.6 (m, −C(O)−CH(C**H$_3$**)−O−). In the IR spectrum of **PS−PLA**, the C=O stretch from **PLA** was observed near 1760 cm^{-1}.

Blend Preparation. Blends were prepared by codissolution of either **PSOH** and **PS−PLA** or two **PS−PLA** diblocks in methylene chloride followed by evaporation of the solvent. The blends were then dried at 105 °C under vacuum. A sample blend comprised of 22 wt % **PSOH(22)** in Table 1 and 78 wt % **PS−PLA** (**SL(52, 0.55)** in Table 2) yielded an average **PLA** volume fraction (f_{PLA}) of 0.42 (**B(40, 0.42)** in Table 2).

Small-Angle X-ray Scattering (SAXS). Before SAXS analysis the samples of powder **PS−PLA**/blends were pressed in a 0.5-mm-thick stainless-steel mold fitted between two Teflon sheets at 140 °C. The SAXS measurements were performed on a home-built beamline at the University of Minnesota. Copper Kα X-rays with a wavelength of 1.542 Å were generated by a Rigaku RU-200BVH rotating anode X-ray machine fitted with a 0.2 × 2-mm^2 microfocus cathode and Franks mirror optics. The temperature of the sample was controlled by an electrically heated brass block, which can be water-cooled, located inside of the evacuated sample chamber. Two-dimensional (2-D) diffraction patterns were recorded using a Siemens multiwire area

(38) Gilman, H.; Cartledge, F. K. *J. Organomet. Chem.* **1964**, *2*, 447−454.
(39) Schmidt, S. C.; Hillmyer, M. A. *Macromolecules* **1999**, *32*, 4794−4801.

Table 2. Characterization of **PS−PLA** Samples

sample[a]	M_n (kg/mol) PS[b]	M_n (kg/mol) PLA[c]	M_n (kg/mol) total	M_w/M_n[d]	f_{PLA}[e]	N[f]	morphology and order–disorder transition temperatures (°C)[g]
SL(10, 0.45)	4.9	4.6	9.5	1.11	0.45	78	L 116 → DIS
SL(12, 0.54)	4.9	6.6	12	1.15	0.54	93	L 164 → DIS
SL(15, 0.43)	8.0	6.9	15	1.07	0.43	123	L 213 → DIS
SL(15, 0.44)	8.0	7.3	15	1.12	0.44	126	L 216 → DIS
SL(18, 0.52)	8.0	9.9	18	1.09	0.52	146	L 268 → DIS
SL(19, 0.54)	8.0	11	19	1.22	0.54	152	L 258 → DIS
SL(38, 0.49)	18	20	38	1.19	0.49	306	L[h]
SL(41, 0.53)	18	23	41	1.22	0.53	333	L[h]
SL(52, 0.55)	22	30	52	1.25	0.55	422	L[h]
SL(107, 0.44)	56	51	107	1.10	0.44	877	L[h]
SL(114, 0.47)	56	58	114	1.17	0.47	930	L[h]
SL(10, 0.45)	56	80	136	1.11	0.55	1100	L[h]
B(15, 0.42)[j]	8.0	6.6	15		0.42	121	G[i]
B(15, 0.41)[j]	8.0	6.5	15		0.41	120	G 185 → DIS
B(14, 0.40)[j]	8.0	6.2	14		0.40	118	G[i]
SL(12, 0.23)	9.0	3.1	12	1.05	0.23	103	C[i]
SL(13, 0.36)	8.0	5.3	13	1.15	0.36	111	C 165 → DIS
SL(23, 0.21)	18	5.5	23	1.10	0.21	197	C[i]
SL(25, 0.26)	18	7.2	25	1.33	0.26	210	C[h]
SL(28, 0.21)	22	6.6	28	1.05	0.21	242	C[h]
SL(32, 0.28)	22	9.9	32	1.06	0.28	267	C[h]
SL(33, 0.31)	22	11	33	1.06	0.31	277	C[h]
SL(36, 0.36)	22	14	36	1.11	0.36	300	C[h]
SL(37, 0.38)	22	15	37	1.10	0.38	307	C[h]
B(40, 0.42)[k]	22	18	40		0.42	330	C[h]
SL(41, 0.43)	22	19	41	1.33	0.43	346	C[h]
SL(58, 0.38)	34	24	58	1.10	0.38	477	C[h]
SL(92, 0.36)	56	36	92	1.16	0.36	763	C[h]
SL(11, 0.13)	9.0	1.5	11	1.03	0.13	90	DIS
SL(11, 0.25)	8.0	3.1	11	1.05	0.25	94	DIS
SL(24, 0.09)	22	2.5	24	1.09	0.09	211	DIS

[a] **SL(*X*,*Y*) = PS−PLA** with total molecular weight (***X*** kg/mol) and f_{PLA} (***Y***). [b] See Table 1. [c] Molecular weight of **PLA** was determined using the N_{PS}/N_{PLA} ratio obtained through ^{1}H NMR spectroscopy and previously determined N_{PS} (see Table 1). [d] SEC versus polystyrene standards. [e] $f_{PLA} = N_{PLA}(N_{PLA} + N_{PS})$. [f] $N = N_{PS} + N_{PLA}$. [g] The morphology (L = lamellae, G = gyroid, C = cylinders, and DIS = disordered) was determined by SAXS at room temperature with the transition temperatures obtained through rheological measurements. [h] Sample remained ordered up to 270 °C by rheology. Samples were exposed to temperatures above 240 °C for only short periods of time to limit the degradation of **PLA** (SEC confirmed that little degradation occurred). [i] Samples were not analyzed by rheology; as a result, their T_{ODT} values are unknown. [j] Blends of **SL(13, 0.36)** and **SL(15, 0.43)**. [k] Blend of **SL(52, 0.55)** and **PSOH(22)** in Table 1.

detector and corrected for detector response before analysis. The 2-D images were azimuthally integrated to a 1-D plot of intensity versus q where $q = 4\pi\lambda^{-1}\sin(\theta/2)$ and θ and λ are the scattering angle and X-ray wavelength, respectively. For quantitative measurement of macroscopic orientation the 2-D images were reduced to a 1-D plot of intensity versus azimuthal angle, β, by summing the intensity of a band, Δq, equal to the full-width-at-half-maximum of the principal peak (q^*).

Microstructural Alignment. The block copolymers/blends that exhibited a hexagonally packed cylindrical morphology were aligned through either reciprocating shear or shear flow. The block copolymers were subjected to reciprocating shear using a Rheometrics RSA II rheometer in the shear-sandwich configuration. Typical conditions for the reciprocating shear were a 0.5-mm sample thickness, 160 °C, 99% strain, and 0.5 rad/s shear frequency. Frequency sweeps before and after subjection to reciprocating shear were performed at 2% strain (within the linear viscoelastic regime for these polymers), 160 °C and frequencies between 0.01 and 100 rad/s.

Subjecting the block copolymers to flow to orient them was done using two techniques. The first involved extruding a block copolymer through a Göttfert Rheo-Tester 1500 capillary rheometer. The polymer is aligned by forcing it through a hollow tube at an elevated temperature and a controlled rate. A typical experimental run was done with a 30-mm-gauge length, 1-mm-diameter orifice, and 160 °C at a flow rate of 1 mm/s.

The use of a channel die to align block copolymers through shear flow has been used previously.[40] Similarly, the morphology of the **PS−PLA** block copolymers was aligned using a home-built channel die 3 mm wide and 60 mm long. Previously pressed pieces of **PS−PLA** were placed in the center of the channel die (channel and bottom of plunger were lined with Teflon sheets) which was then heated to the desired temperature (115−140 °C) in a laboratory press. The polymer was subjected to compression causing it to flow toward the ends of the channel. Typical compression ratios used in these channel die experiments ranged from 6 to 15. The samples were allowed to cool to 50 °C over a period of 1 h before the applied load was released and the aligned material was removed from the die with sample thickness between 0.5 and 3 mm. The degree of alignment in all cases was determined by SAXS.

Degradation of PLA in PS−PLA Samples. A 0.5 M solution was prepared by dissolving 2.0 g of sodium hydroxide (Aldrich) in an 40/60 (by volume) solution of methanol/water (total volume of 100 mL). The degradations were done by placing a **PS−PLA** sample (either pressed or aligned) in the solution and then stirring in an oil bath at 65 °C. The length of time that the sample was subjected to these conditions varied, but typically degradations were carried out for about a week. After the degradation was stopped, the sample was washed with water and methanol and was then dried under vacuum for 14 h at room temperature. The degradation of **PLA** from the samples was followed by ^{1}H NMR spectroscopy and SEC.

Scanning Electron Microscopy (SEM). SEM samples were prepared by either fracturing or cutting the porous monoliths which were then mounted to brass shims using CCC Carbon Adhesive (Electron Microscopy Sciences). The samples were sputter-coated with 2−3 nm

(40) Drzal, P. L.; Barnes, J. D.; Kofinas, P. *Polymer* **2001**, *42*, 5633−5642.

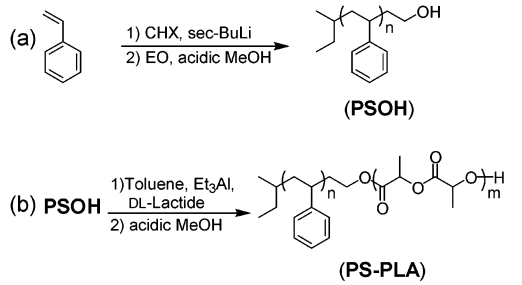

Figure 2. (a) Anionic polymerization of styrene and end-functionalization with ethylene oxide (EO). (b) Formation of the macroinitiator followed by the controlled polymerization of D,L-lactide to form **PS−PLA**.

of platinum (the platinum coating thickness is estimated from a calculated deposition rate and experimental deposition time) before being analyzed on a Hitachi S-900 FE-SEM using accelerating voltages of 2−5 keV.

Nitrogen Adsorption. The measurements were performed on a Micromeritics ASAP 2000 V3.00 sorption analyzer or on a TCM-100 sorption system (Advanced Scientific Designs, Inc.). Surface area calculations were made using the Brunauer−Emmett−Teller (BET),[41,42] method while the pore volume and pore size distributions were determined from Barrett−Joyner−Halenda (BJH)[42,43] calculations utilizing the adsorption portion of the isotherm.

End-Functionality. Porous **PS** monoliths were submerged in trifluoroacetic anhydride (Aldrich) for 2 days. The monoliths were then washed and soaked in methanol for 2 days to ensure that all the excess trifluoroacetic anhydride had been removed from the voids. They were then vacuum-dried at room temperature for 1 day. The formation of the ester linkage was followed by IR and ^{1}H NMR spectroscopy. The trifluoroester-functionalized **PS** showed a (b, PS−CH_2−C**H_2**−O−C(O)−CF_3) resonance at 4.0 ppm in the ^{1}H NMR spectrum and a C═O stretch at 1786 cm^{-1} in the IR spectrum.

Results & Discussion

Synthesis of PS−PLA. Well-defined block copolymers of **PS−PLA** were synthesized through the combination of living anionic polymerization and controlled coordination insertion polymerization.[39] Living anionic polymerization was used for the polymerization of styrene which was endcapped with ethylene oxide (EO) to yield **PSOH** (Figure 2a). The **PSOH** samples exhibited narrow molecular weight distributions by SEC and high hydroxyl end-group functionalization by ^{1}H NMR spectroscopy confirming the controlled-nature of this polymerization (Table 1).[37] Quirk et al.[44,45] have shown that this reaction results in the monoaddition of EO with complete efficiency provided that [EO]/[polystyryllithium] ≤ 4. While the conditions ([EO]/[polystyryllithium] > 4) used in the polymerization of the **PSOH** samples presented in this report may result in oligomerization, little or none was observed by ^{1}H NMR spectroscopy. The molecular weights of the **PSOH** samples and subsequently, **PS−PLA** samples, were determined by ^{1}H NMR spectroscopy through end-group analysis. These molecular weights were used in all further calculations.

Aluminum alkoxides have been used for the ring-opening polymerization of lactide to produce controlled molecular weight polymers with narrow chain-length distributions.[39,46,47] For our system, triethylaluminum was used to convert the **PSOH** to the corresponding aluminum alkoxide macroinitiator.[39,48] This macroinitiator was then used in the ring-opening polymerization of D,L-lactide to obtain **PS−PLA** (Figure 2b). The resulting diblocks were amorphous since **PS** synthesized by the methods employed here is atactic and the use of D,L-lactide gives atactic **PLA**,[49] the latter being important in the degradation of **PLA**.[50] An increase in the molecular weight after the lactide polymerization by SEC confirmed the formation of a diblock copolymer.[37] Furthermore, all block copolymers had narrow molecular weight distributions, M_w/M_n typically ≤1.2. By varying the conversion of lactide, the molecular weight/volume fraction of the **PLA** segment was readily controlled, yielding command of the resulting morphology. The molecular characteristics for the **PS−PLA** samples explored in this study are listed in Table 2.

Morphology Diagram. For diblock copolymers, four equilibrium morphologies have been identified: lamellae (L), bicontinuous gyroid (G), hexagonally packed cylinders (C), and spheres on a body-centered cubic lattice (S).[51,52] The equilibrium morphology of a diblock copolymer generally depends on two factors: the product of the overall degree of polymerization and the Flory−Huggins interaction parameter, χN, and the composition, f.[52] The two parameters, N and f, affect the entropy of mixing, whereas the χ parameter, which is largely a measure of the contact energy between the chemically different polymer segments, is mostly enthalpic in nature.[51] The temperature dependence of χ is typically described by:

$$\chi(T) = \frac{\alpha}{T} + \beta \qquad (1)$$

where α is an enthalpic coefficient and β is an excess entropic coefficient.[2] By varying temperature, the value of χ and, as a result, the morphological state of the system can be controlled. As χ increases, the system segregates into domains, each rich with one of the components, to reduce the number of contacts between the different polymers. This segregation is accompanied by a loss in entropy due to the resultant chain-stretching and localization of the block junctions. At χN values ≤10, entropy dominates, and the block copolymer exists in a disordered state. As χN increases, the block copolymer segments segregate (predicted to be at $\chi N = 10.5$ for a symmetric diblock copolymer[53]), and the point at which this segregation occurs is the order−disorder transition (ODT). The polymer segments are covalently linked and, as a result, phase-separate into ordered nanodomains.

The morphology that results is largely determined by the amount of stretching each block undergoes as dictated by the packing frustrations imposed for different values of f.[51] For equal

(41) Brunauer, S.; Emmett, P. H.; Teller, E. *J. Am. Chem. Soc.* **1938**, *60*, 309−319.
(42) Gregg, S. J.; Sing, K. S. W. *Adsorption, Surface Area and Porosity*; Academic Press: London, 1982.
(43) Barrett, E. P.; Joyner, L. G.; Halenda, P. P. *J. Am. Chem. Soc.* **1951**, *73*, 373−380.
(44) Quirk, R. P.; Ma, J.-J. *J. Polym. Sci., Part A: Polym. Chem.* **1988**, *26*, 2031−2037.
(45) Quirk, R. P.; Mathers, R. T.; Wesdemiotis, C.; Arnould, M. A. *Macromolecules* **2002**, *35*, 2912−2918.
(46) Kricheldorf, H.; Berl, M.; Scharnagle, N. *Macromolecules* **1988**, *21*, 286−293.
(47) Dubois, P.; Jerome, R.; Teyssie, P. *Makromol. Chem., Macromol. Symp.* **1991**, *42/43*, 103−116.
(48) Wang, Y.; Hillmyer, M. A. *Macromolecules* **2000**, *33*, 7395−7403.
(49) Thakur, K. A. M.; Kean, R. T.; Hall, E. S.; Doscotch, M. A.; Munson, E. J. *Anal. Chem.* **1997**, *69*, 4303−4309.
(50) Li, S. *J. Biomed. Mater. Res.* **1999**, *48*, 342−353.
(51) Bates, F. S. *Science* **1991**, *251*, 898−905.
(52) Bates, F. S.; Fredrickson, G. H. *Phys. Today* **1999**, 32−38.
(53) Leibler, L. *Macromolecules* **1980**, *13*, 1602−1617.

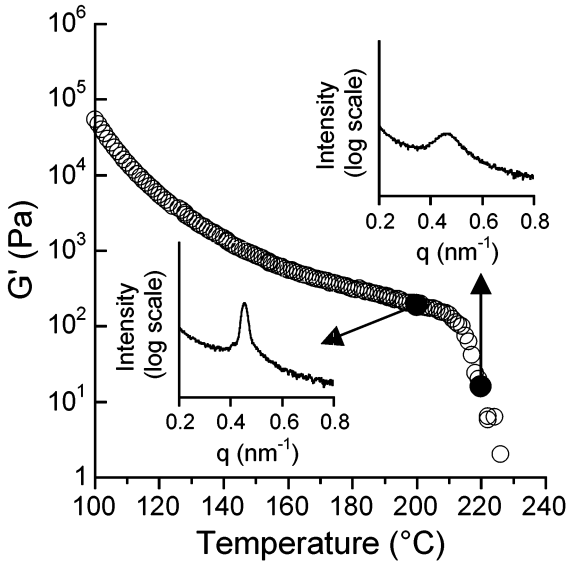

Figure 3. Temperature dependence of the dynamic storage modulus (G′) for **SL(15, 0.43)** in Table 2 (1 °C/min, 0.5 rad/s, and 2% strain). An order-disorder transition is indicated by the discontinuous decrease in G′ ($T_{ODT} \approx 213$ °C). The inset 1-D SAXS patterns further confirm this disordering by the observation of principal peak broadening at temperatures above the T_{ODT}.

volume fractions ($f = 0.5$), the blocks stretch about equal distances, resulting in flat interfaces or a lamellar morphology. But for block copolymers with different values of *f*, each of the chains stretch different amounts to form the most energetically favorable arrangement. For example, for the cylindrical morphology, the longer block resides on the convex side of the block copolymer interface. This arrangement results in the longer block gaining configurational entropy, which outweighs the loss in entropy of the shorter blocks. The ability to control the self-assembly of block copolymers into various morphologies and the fact that spatially periodic structures result render block copolymers ideal candidates for making nanostructured materials.

To effectively use **PS−PLA** materials as precursors to nanoporous polymers, a knowledge of the morphological behavior is necessary. The most efficient method to do this is to synthesize block copolymers with differing *N* and *f* values and determine the temperature dependence of χ. While the degree of polymerization and the composition can be controlled synthetically, the $\chi(T)$ parameter is determined by the monomers that comprise the blocks. As a result, a series of block copolymers of different degrees of polymerization and compositions (Table 2) were synthesized, and an expression for $\chi(T)$ was formulated so that a morphology diagram (χN vs f_{PLA}) for **PS−PLA** could be constructed.

The morphologies for a series of **PS−PLA** samples (Table 2) were determined by SAXS at various temperatures at and above 110 °C to avoid nonequilibrium effects below the glass-transition of **PS**. In addition, some of the samples exhibited ODTs. Sharp decreases in the dynamic elastic modulus (G') during dynamic mechanical measurements have been used to locate ODT temperatures (T_{ODT}).[54−56] These transitions for **PS−PLA** were studied by measuring the temperature dependence

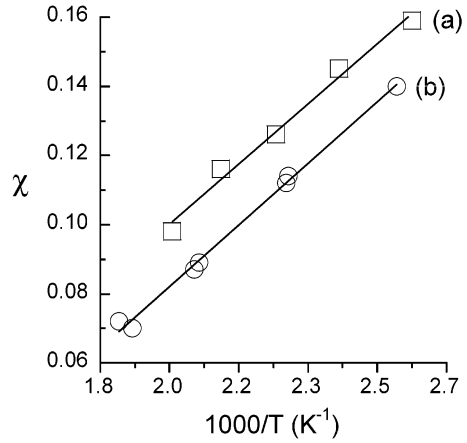

Figure 4. Temperature dependence of χ: (a) determined through the change in D_{lam} with temperature for **SL(38, 0.49)** in Table 2. A linear fit to the data gave: $\chi(T) = 96.6/T - 0.091$. (b) extracted from rheologically determined T_{ODT} values for **SL(10, 0.45)**, **SL(12, 0.54)**, **SL(15, 0.43)**, **SL(15, 0.44)**, **SL(18, 0.52)**, **SL(19, 0.54)**, and **SL(13, 0.36)** in Table 2 along with their predicted $(\chi N)_{ODT}$ values.[26] A linear fit to the data gave: $\chi(T) = 98.1/T - 0.112$.

of G' for many of these block copolymers (Figure 3) with the T_{ODT} values given in Table 2. The values of the T_{ODT}'s were verified by SAXS through principal peak (q^*) broadening at temperatures above the T_{ODT} (Figure 3, insets).[57] These T_{ODT} values were later used in the determination of the temperature dependence of χ.

Finding $\chi(T)$ for a block requires the comparison of independently determined expressions to test its validity. As a result, an expression for the $\chi(T)$ of **PS−PLA** was found experimentally by two different methods. Matsen and Bates,[58] through the use of self-consistent mean-field theory, have developed a theoretical morphology diagram that predicts the value of χN at the ODT as a function of *f*. Values of χ at the T_{ODT} for a series of **PS−PLA** samples of known *N* and *f* (Table 2) were extracted from this theoretical morphology diagram. These extracted χ values for specific temperatures were used to determine the temperature dependence of χ which is plotted in Figure 4b and is described by eq 2.

$$\chi(T) = \frac{98.1}{T} - 0.112 \tag{2}$$

Another method for determining χ is by measuring the characteristic domain spacing (*D*). In ordered block copolymers, the characteristic spacing for the spherical, cylindrical, and lamellar morphologies has been shown to have the same functional dependence on the statistical segment length (*a*), *N* and χ.[59] The exact characteristic domain spacing for the lamellar morphology (at $f = 0.5$) in the strong-segregation regime ($\chi N \geq 100$) is given by:

$$D_{lam} = 1.10 a N^{2/3} \chi^{1/6} \tag{3}$$

To determine χ, the values of D_{lam}, *a*, and *N* are required. The characteristic domain spacing, D_{lam}, was obtained from SAXS

(54) Rosedale, J. H.; Bates, F. S. *Macromolecules* **1990**, *23*, 2329−2338.
(55) Hamley, I. W.; Koppi, K. A.; Bates, F. S.; Almdal, K.; Mortensen, K. *Macromolecules* **1993**, *26*, 5959−5970.
(56) Khandpur, A. K.; Förster, S.; Bates, F. S.; Hamley, I. W.; Ryan, A. J.; Bras, W.; Almdal, K.; Mortensen, K. *Macromolecules* **1995**, *28*, 8796−8806.
(57) Rosedale, J. H.; Bates, F. S.; Almdal, K.; Mortensen, K.; Wignall, G. D. *Macromolecules* **1995**, *28*, 1429−1443.
(58) Matsen, M. W.; Bates, F. S. *Macromolecules* **1996**, *29*, 1091−1098.
(59) Semenov, A. N. *Sov. Phys. JETP* **1985**, *61*, 733−742.

using the expression:

$$q^* = \frac{2\pi}{D_{\text{lam}}} \tag{4}$$

where q^* is the position of the principal peak. The average statistical segment length for the **PS−PLA** block copolymer (a_{SL}) was determined from:

$$a_{SL} = \left(\frac{f_{PS}}{a_{PS}^2} + \frac{f_{PLA}}{a_{PLA}^2}\right)^{-1/2} \tag{5}$$

where f_{PS} and f_{PLA} are volume fractions of each block with the statistical segment lengths $a_{PS} = 7.1$ Å[60] and $a_{PLA} = 10.2$ Å[61] after correction for a reference volume of 185 Å^3.

The characteristic spacing changes with temperature and can be followed by the change in q^* (eq 4) with temperature by SAXS. The q^* values at different temperatures for **SL(38, 0.49)** in Table 2 were determined, and the corresponding values of χ were calculated from eq 3. The change in the statistical segment length with temperature is generally weak.[62] Also, a change in temperature for these materials does not significantly alter f (for **SL(38, 0.49)** in Table 2, f_{PLA} (110 °C) = 0.492 and f_{PLA} (200 °C) = 0.494). As a result, these effects were ignored in the determination of χ from eq 3. Although eq 3 is only strictly valid in the strong-segregation regime, the deviation associated with its application to the intermediate-segregation regime is relatively small and becomes less significant as χN increases within this region.[63] This sample ($\chi N \approx 50$ at $T = 110$ °C) falls within the upper limits of the intermediate-segregation regime and therefore should provide a reasonable estimate for χ from eq 3. A plot of χ versus $1/T$ is shown in Figure 4a and is described by eq 6.

$$\chi(T) = \frac{96.6}{T} - 0.091 \tag{6}$$

This expression is nearly identical to eq 2 determined from the theoretical morphology diagram and T_{ODT} values. The true expression for $\chi(T)$ probably lies between eqs 2 and 6. While theory predicts that the ODT for a symmetric block copolymer should occur at $\chi N = 10.5$, composition fluctuations result in the system being disordered at $\chi N > 10.5$.[64,65] As a result, the χ values extracted from the theoretical phase diagram and calculated from eq 2 may be artificially low. While $\chi(T)$ may be underestimated in eq 2, eq 6 may overstate the value of χ. The **PS−PLA** sample used for this calculation falls within the intermediate-segregation regime which has been shown to have domain spacing proportionalities to molecular weight greater than $^2/_3$.[66−68] This would result in χ being too high when calculated from eq 3 and likewise, eq 6.

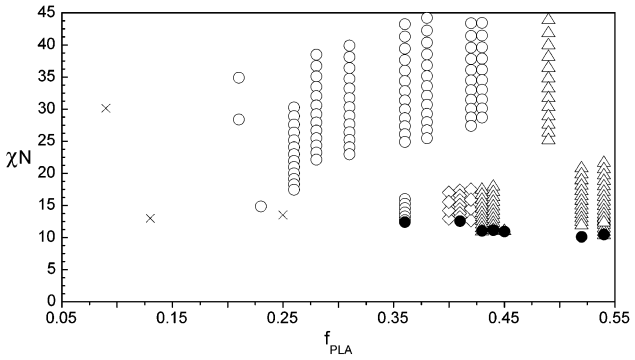

Figure 5. Experimental **PS−PLA** morphology diagram. Morphologies were determined from SAXS at different temperatures (circles = cylinders, diamonds = gyroid, triangles = lamellae and crosses = disordered) with solid circles indicating order−disorder transitions determined from rheology.

To test the experimentally determined $\chi(T)$ further, a series of **PS−PLA** block copolymers (**SL(41, 0.53)**, **SL(52, 0.55)**, **SL(107, 0.44)**, **SL(114, 0.47)**, and **SL(136, 0.55)** in Table 2) exhibiting the lamellar morphology and of high enough N to avoid significant fluctuation effects were analyzed by SAXS at 110 °C using eq 3 giving an average $\chi = 0.15 \pm 0.03$. This value lies between the predicted value at 110 °C from eq 2, 0.14 and eq 6, 0.16 as may have been expected from the above discussion. These results indicate a moderate interaction strength between **PS** and **PLA**, only slightly higher than that of **PS−**polyisoprene.[56] However, the value of χ for **PS−PLA** is smaller by more than a factor of 3 than that in the related poly(ethylene-*alt*-propylene)−**PLA** system.[69]

With the expression for $\chi(T)$ determined from the ODT measurements (eq 2), a **PS−PLA** morphology diagram (χN vs f_{PLA}) was constructed for f_{PLA} values between 0.05 and 0.55 (Figure 5). Equation 2 was chosen for $\chi(T)$ because it was determined from a wider range of **PS−PLA** samples of differing f values than eq 6. For each of the open points in Figure 5, the morphology was determined by SAXS at a specific temperature. This was then used along with eq 2 to calculate the corresponding χN that was plotted against its f_{PLA}. The morphology diagram shows C, G, and L. We did not definitively identify the spherical morphology in this system. The boundaries between order and disorder determined by rheology are designated by solid circles on the morphology diagram. Included in the morphology diagram are three samples, **SL(11, 0.13)**, **SL(11, 0.25)**, and **SL(24, 0.09)** in Table 2, in the disordered state to further aid in mapping out the areas of disorder. The two morphologies that are useful for making porous materials for **PLA**-containing block copolymers are C and G because the minor component can be removed and the major component forms a continuous matrix. The cylindrical morphology was observed for **PS−PLA** in the intermediate-segregation regime between f_{PLA} values of 0.21 and 0.43.[70] With such a large target, this system affords versatility in making microdomains of different sizes and spacings. With this in mind, a series of block copolymers varying in both chain length and **PLA** content were prepared while maintaining the cylindrical morphology.

(60) Fetters, L. J.; Lohse, D. J.; Richter, D.; Witten, T. A.; Zirkel, A. *Macromolecules* **1994**, *27*, 4639−4647.
(61) Joziasse, C. A.; Veenstra, H.; Grijpma, D. W.; Pennings, A. *Macromol. Chem. Phys.* **1996**, *197*, 2219−2229.
(62) Boothroyd, A. T.; Rennie, A. R.; Wignall, G. D. *J. Chem. Phys.* **1993**, *99*, 9135−9144.
(63) Matsen, M. W.; Bates, F. S. *J. Chem. Phys.* **1997**, *106*, 2436−2448.
(64) Fredrickson, G. H.; Helfand, E. *J. Chem. Phys.* **1987**, *87*, 697−705.
(65) Bates, F. S.; Rosedale, J. H.; Fredrickson, G. H.; Glinka, C. *Phys. Rev. Lett.* **1988**, *61*, 2229−2232.
(66) Hadziioannou, G.; Skoulios, A. *Macromolecules* **1982**, *15*, 258−262.
(67) Almdal, K.; Rosedale, J. H.; Bates, F. S.; Wignall, G. D.; Fredrickson, G. H. *Phys. Rev. Lett.* **1990**, *65*, 1112−1115.
(68) Foster, M. D.; Sikka, M.; Singh, N.; Bates, F. S.; Satija, S. K.; Majkrzak, C. F. *J. Chem. Phys.* **1992**, *96*, 8605−8615.
(69) Schmidt, S. C.; Hillmyer, M. A. *J. Polym. Sci., Part B: Polym. Phys.* **2002**, *40*, 2364−2376.
(70) A small region of the bicontinuous morphology, gyroid, was also found between f_{PLA} values of 0.40 and 0.42 at low χN through the blending of two block copolymers, **SL(15, 0.43)** and **SL(13, 0.36)** in Table 2.

Microstructural Alignment. The use of flow to induce macroscale order in block copolymers was first explored by Keller.[71−73] Many methods to orient block copolymers have been demonstrated including extrusion,[74] oscillatory shear,[75,76] roll-casting,[77,78] electric fields,[31,79] and temperature gradients.[80] Subjecting block copolymers to flow fields, as in the case of reciprocating shear or shear flow (e.g., channel die processing), provides a method for inducing macroscale order into bulk materials. When block copolymers are subject to shear deformation, a shear stress is induced. The material will rearrange to relieve this stress. For a sample of cylindrical morphology, the alignment of the cylinders coincident along the direction of the shear relieves the stress forming a macroscopically oriented sample. **PS−PLA** samples were aligned, using both reciprocating shear as well as shear flow through the use of a channel die or extrusion through a capillary rheometer.

Pressed **PS−PLA** (0.5-mm-thick) samples were aligned through reciprocating shear at a frequency (ω) of 0.5 rad/s, 99% strain and 160 °C, typically for 4 h. The alignment was tracked by comparing frequency sweeps ($100 \geq \omega \geq 0.01$ rad/s, 2% strain and 160 °C) both before and after the block was subjected to extended periods of reciprocating shear. Alignment alters the relaxation behavior of a block copolymer material such that the post-shear modulus at low frequency is less than the pre-shear response.[81] For all of the samples we aligned using reciprocating shear this was true (e.g., for one sample subjected to the conditions above, the pre-shear modulus was 9.0×10^3 Pa at $\omega = 0.01$ rad/s compared to a post-shear response of 1.6×10^3 Pa). We also showed previously the 2-D SAXS patterns resulting from a shear-aligned sample which exhibited a two-spot pattern in the shear gradient direction and a six-spot pattern in the shear direction as is expected for a well-aligned sample.[37] These samples also exhibited the same two-spot and six-spot 2-D SAXS patterns.

While reciprocating shear yielded well-aligned samples, it is both time-exhaustive and limiting in sample size and shape. To overcome these limitations, the use of shear flow as a means to induce alignment either through channel die processing or passage through a capillary rheometer was investigated. A typical experimental run with the capillary rheometer was carried out using a 30-mm-gauge length, 1-mm-diameter orifice, at 160 °C, and with a flow rate of 1 mm/s. The rods of **PS−PLA** contained **PLA** cylinders aligned in the direction of shear. Similarly, channel die processing the block copolymer aligns the cylinders coincident with the shear direction.[40] The channel die process consisted of heating **PS−PLA** in a laterally confining chamber to a desired temperature (115−140 °C) and then compressing it (to the desired thickness and compression ratio) such that it flowed toward the ends of the channel die. The resulting rectangular piece ($60 \times 3 \times 1$ mm^3) was cooled slowly before it was removed. Alignment in all of the processed samples was evaluated and quantified by SAXS.

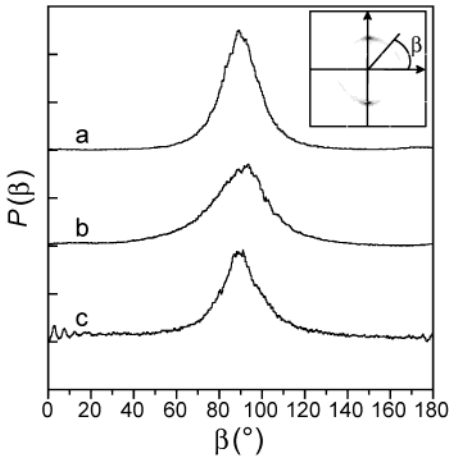

Figure 6. Normalized orientation distribution function ($P(\beta)$) for **SL(37, 0.38)** in Table 2 aligned through: (a) channel die processing at 140 °C with a compression ratio of 8 ($F_2 = 0.85$). (b) reciprocating shear at 160 °C, $\omega = 0.5$ rad/s, 99% strain for 4 h ($F_2 = 0.73$). (c) extrusion from a capillary rheometer at 160 °C and a flow rate of 1 mm/s ($F_2 = 0.63$). The azimuthal angle (β) is measured from the direction parallel to the cylinders axes as shown in the inset.

To compare the degree of orientation of the three methods, the second-order orientation factor (F_2) was calculated from the 2-D SAXS patterns in the shear gradient direction.[82−84] Azimuthal scans were performed on these patterns radially along the first-order peak position (q^*) to obtain the scattering intensity as a function of azimuthal angle (β). The angle, β, was measured from the direction parallel to the cylinders axes and the intensity was integrated centered at q^* and limited by the full-width-at-half-maximum of the first-order peak (Figure 6, inset). The normalized orientation distribution function ($P(\beta)$) where $I(q^*,\beta)$ is the scattering intensity is given by eq. 7.

$$P(\beta) = \frac{I(q^*,\beta)q^{*2}}{\int_0^\pi I(q^*,\beta)q^{*2}\sin\beta d\beta} \tag{7}$$

Figure 6 shows the normalized orientation distribution function for representative samples of each alignment method. F_2 was then calculated as shown in eq 8.

$$F_2 = 1 - 3\langle\cos^2\beta\rangle \tag{8}$$

where $\langle\cos^2\beta\rangle$ is defined as:

$$\langle\cos^2\beta\rangle = \int_0^\pi \cos^2\beta P(\beta)\sin\beta d\beta \tag{9}$$

Under the conditions previously reported, the reciprocating shear consistently produced rectangular-shaped samples with orientation factors of 0.7. In contrast, the capillary rheometer allowed

(71) Keller, A.; Pedemonte, E.; Wilmouth, F. M. *Kolloid Z. Z. Polym.* **1970**, *238*, 385−389.
(72) Keller, A.; Pedemonte, E.; Wilmouth, F. M. *Nature* **1970**, *225*, 538−539.
(73) Folkes, M. J.; Keller, A.; Scalisi, F. P. *Kolloid Z. Z. Polym.* **1973**, *251*, 1−4.
(74) Hadziioannou, G.; Mathis, A.; Skoulios, A. *Colloid Polym. Sci.* **1979**, *257*, 136−139.
(75) Bates, F. S.; Koppi, K. A.; Tirrell, M.; Almdal, K.; Mortensen, K. *Macromolecules* **1994**, *27*, 5934−5936.
(76) Chen, Z.-R.; Kornfield, J. A.; Smith, S. D.; Grothaus, J. T.; Satkowsdi, M. M. *Science* **1997**, *277*, 1248−1253.
(77) Albalak, R. J. *Polymer* **1994**, *35*, 4115−4119.
(78) Albalak, R. J.; Thomas, E. L. *J. Polym. Sci., Part B: Polym. Phys.* **1994**, *32*, 341−350.
(79) Mansky, P.; DeRouchey, J.; Russell, T. P.; Mays, J.; Pitsikalis, M.; Morkved, T.; Jaeger, H. *Macromolecules* **1998**, *31*, 4399−4401.
(80) Bodycomb, J.; Funaki, Y.; Kimishima, K.; Hashimoto, T. *Macromolecules* **1999**, *32*, 2075−2077.
(81) Patel, S. S.; Larson, R. G.; Winey, K. I.; Watanabe, H. *Macromolecules* **1995**, *28*, 4313−4318.
(82) deGennes, P. G.; Prost, J. *The Physics of Liquid Crystals*; Oxford University Press: New York, 1993.
(83) Sakurai, S.; Aida, S.; Okamoto, S.; Ono, T.; Imaizumi, K.; Nomura, S. *Macromolecules* **2001**, *34*, 3672−3678.
(84) Pople, J. A.; Hamley, I. W.; Fairclough, J. P. A.; Ryan, A. J.; Booth, C. *Macromolecules* **1998**, *31*, 2952−2956.

us to produce long rod-shaped samples. These samples are easier to handle due to their shape and size. Nevertheless, the orientation factors of these samples were typically 0.1 less than those produced by the reciprocating shear. Samples subjected to channel die processing yielded the best aligned pieces with orientation factors typically greater than 0.8.[85]

The alignment of the cylindrical morphology in a channel die-processed piece was evaluated using SAXS at regularly spaced places throughout a sample (pressed with a compression ratio of 6 to a thickness of 1 mm at 125 °C) both in the direction of shear and laterally (Figure S1). The analysis showed that high alignment is maintained throughout the entire piece with the exception of a small portion near the center of the piece, corresponding to the area of loading in the channel die. Presumably this is due to the material not being subjected to the same magnitude of shear flow in the center as that toward the ends of the channel die. However, the F_2 in the middle is not zero but 0.66, indicating that the cylinders are still exhibiting a preference to align in the shear direction. These results do show that pieces of up to 2.5 cm in length (if the middle portion is removed) with various thicknesses and high alignment throughout can be made by channel die processing. This high alignment suggests that upon removal of **PLA**, it is likely that a pathway through the sample will exist. Thus, the channel die proved to be the best method of alignment not only due to the highly oriented pieces of various thicknesses it produced but also because of the technical simplicity.

Degradation of PLA in Ordered PS−PLA Monoliths. Porous materials were prepared from **PS−PLA** block copolymers exhibiting the cylindrical morphology by removal of the **PLA**. A mild degradation route for the removal of **PLA** is necessary so that the structural integrity of the **PS** matrix is not compromised. **PLA** is known to be hydrolytically unstable as well as susceptible to thermal degradation at temperatures higher than 200 °C.[50,86−88] The glass-transition temperatures of the **PSOH** samples were found to be about 100 °C by DSC; thus, at the elevated temperatures necessary for thermal degradation of **PLA** the **PS** would flow. As a result, hydrolytic degradation was used.

Most studies of the hydrolytic degradation of **PLA** have been done for biomedical uses, and typical degradation media mimic biological conditions.[50] These studies have shown that the half-life of **PLA** in this situation is about 10 weeks.[89] The use of hydroxide anions has been found to increase the rate of hydrolytic degradation of **PLA**,[50] and we employed a related method. **PS−PLA** pieces were placed in a 0.5 M sodium hydroxide water/methanol solution. The system was heated to 65 °C, above the glass-transition temperature of **PLA**, to increase the degradation rate while keeping the temperature well below the glass-transition temperature of **PS**. The **PS** is insoluble in this solution; however, the degradation product, sodium lactate, is soluble, ensuring that the minor component is removed from the precursor while not harming the matrix.

To test this degradation regimen, it was applied to as-pressed **PS−PLA** samples. However, initial degradations were very slow (little degradation after a week), and the pieces typically fractured. These results were not surprising for no further steps were employed to align these as-pressed samples; thus, the **PLA** domains are unaligned with grain boundaries between them, as evidenced by the isotropic ring at q^* for the 2-D SAXS analyses of these samples. The fragmentation could be attributed to different grains being cleaved from one another during the degradation process. Furthermore, a lack of alignment may hamper the degradation of the **PLA** from the samples. Access to all of the **PLA** domains may be sheltered by the **PS** matrix. Aligning the domains to attain macroscale order was the key to obtaining complete degradation without fragmentation as was previously reported.[37] The removal of **PLA** from the monoliths was monitored by SEC and ^{1}H NMR spectroscopy. SEC showed that the degraded pieces had molecular weight distributions identical to their **PSOH** precursors. The lack of a signal due to the methine protons of **PLA** in the ^{1}H NMR spectra was further evidence that the **PLA** was completely removed.

Analysis of Pore Structure. SAXS analysis of typical nanoporous **PS** monoliths showed the same two-spot and six-spot patterns after degradation that were seen previously for the aligned block copolymers.[37] The samples generally had the same orientation factor, consistent with well-ordered and well-aligned nanoporous **PS** monoliths. There was no observable change in the q^* value for the nanoporous material relative to its **PS−PLA** precursor. This indicates that no modification to the matrix occurs during the degradation process and that pore dimensions are dictated by the diblock copolymer. In addition to no change in q^* after degradation, the intensity of the principal scattering peak increased, consistent with the gain in contrast that would be observed by replacing the electron-dense **PLA** fraction with vacuum.[90] These results confirm that the degradation of **PLA** leaves the **PS** matrix unharmed.

Real-space images of the nanoporous monoliths were obtained by high-resolution SEM (Figure 7 shows representative images for a nanoporous monolith obtained from **SL(37, 0.38)** in Table 2). SEM showed that the fractured surface is full of hexagonally packed pores with Figure 7b showing a smaller region of a nanoporous material exhibiting well-ordered voids. A pore size of 16 nm with an average intercylinder spacing of 32 ± 2 nm was ascertained from this SEM image. These dimensions are consistent with the SAXS data after accounting for the Pt coating thickness (ca. 2 nm). Defects are also visible in the SEM images (circled in Figure 7a and c). These defects have consequences on the pore fidelity or the pathway through the voided structure.

Assessing the pore fidelity for application of these porous materials as nanomaterial scaffolds or in understanding the transport properties through the material is important. A sense of the pore fidelity can be assessed from the SEM micrograph of the nanoporous material fractured coincident with the direction of shear shown in Figure 7c. However, the analysis is

(85) On the basis of an approximation accounting for the finite beam size in the analysis of the second-order orientation factor (F_2), the largest F_2 that can be measured is 0.99. None of the samples presented in this paper approached this alignment, and thus the beam-size effect on the analysis was not considered.

(86) Vert, M.; Li, S. M.; Spenlehauer, G.; Guerin, P. *J. Mater. Sci.: Mater. Med.* **1992**, *3*, 432−446.
(87) Huffman, K. R.; Casey, D. J. *J. Polym. Sci., Polym. Chem. Ed.* **1985**, *23*, 1939−1954.
(88) Jamshidi, K.; Hyon, S.-H.; Ikada, Y. *Polymer* **1988**, *29*, 2229−2234.
(89) Li, S.; Garreau, H.; Vert, M. *J. Mater. Sci.: Mater. Med.* **1990**, *1*, 123−130.

(90) SAXS intensity of a diblock copolymer is proportional to the square of the electron density difference between the two phases. The total electron density (in mol e^-/cm^3) = [no. electrons × ρ × (repeat unit molecular weight)$^{-1}$]. The electron density for **PS** = 0.560 mol e^-/cm^3 and for **PLA** = 0.665 mol e^-/cm^3. The electron density for vacuum is approximately 0 mol e^-/cm^3. The expected contrast gain would be $(0.560 - 0)^2/(0.560 - 0.665)^2 = 28$. The observed gain was 24.

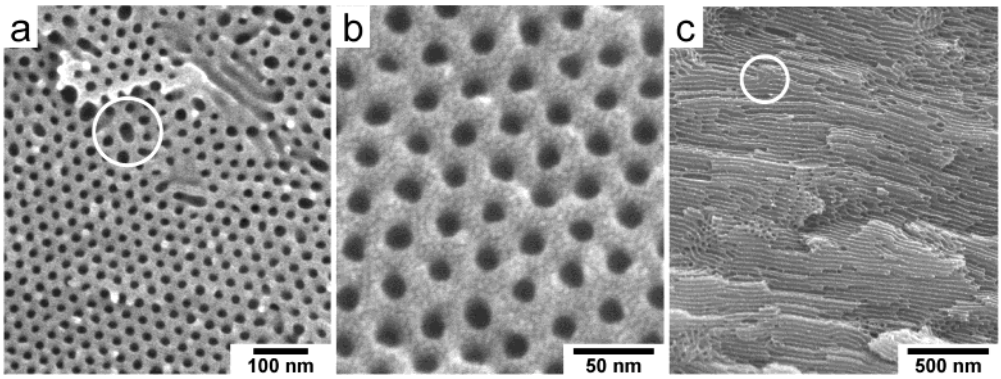

Figure 7. Scanning electron micrographs of porous material obtained using **SL(37, 0.38)** in Table 2 as the precursor. (a) View perpendicular to the cylinder axes. A defect is encompassed by the circle. (b) View perpendicular to the cylinder axes showing a region of highly ordered, hexagonally packed pores. The fine features on the surface are the result of the Pt coating. (c) View parallel to the cylinder axes. A defect is encompassed by the circle.

hampered by the fact that instead of one coplanar set of cylinders being imaged, multiple planes or terraces of channels are observed. As a result the pathway can only be followed to a certain point before it is lost due to its diving underneath another set of channels. Areas showing channels that run the length of at least 4 μm are evident, and presumably the channels have longer unfettered pathways.

To ascertain if a pathway through the entire piece exists, a nanoporous **PS** monolith was mounted with its pores oriented vertically (Figure S2a). A small amount (ca. 2 μL) of a colored methanol solution was applied to this face every 5 min, and its percolation into the pores was monitored.[91] After 2 h the entire monolith was filled. While this is not evidence that each channel runs uninterrupted throughout the entire piece, it does verify that an open pathway does exist in the nanoporous monoliths. Defects such as that circled in Figure 7a where two cylinders have "fused" may provide the connection of the channels necessary to have a continuous pathway. A better view of one these defects is circled in Figure 7c. Places where two cylinders have been conjoined are evident throughout this image. Even though defects exist, the pathways are anisotropic, for the colored solution does not pass through the piece when applied normal to the direction of the channels (Figure S2b).

Modification of Pore Size. Due to the large range of f_{PLA} in which the block copolymer exhibits the cylindrical morphology (Figure 5), the **PS**−**PLA** system can be readily manipulated to give a variety of pore sizes and wall thicknesses. The domain sizes of the original block copolymer precursor dictate the size characteristics of the porous material.[33] The domain sizes are directly modifiable by changing the block copolymer molecular weights (**SL(32, 0.28)**, **SL(37, 0.38)**, **SL(58, 0.38)**, and **SL(92, 0.36)** in Table 2 were all used as precursors to porous materials). The domain spacings were measured by SAXS at 25 °C for this system, and found to scale with $N^{0.81}$ for similar values of f_{PLA} (**SL(37, 0.38)**, **SL(58, 0.38)**, and **SL(92, 0.36)** in Table 2). This result is inconsistent with the dependence of domain spacing on the molecular weight observed by Russell et al.[33] for nanoporous polymer films. They observe a lattice-period dependence on molecular weight of $N^{0.64}$ close to the predicted value of $N^{2/3}$ in the strong-segregation regime. However, most of the **PS**−**PLA** samples presented in this report fall in the weak-/intermediate-segregation regime. Due to chain-stretching as the ODT is approached, the exponential relationship between D and N increases from 2/3, consistent with our findings.[66−68]

Another method to change pore size is through blending. Block copolymers are able to incorporate small amounts of homopolymer without macrophase separation into the corresponding domain. The added homopolymer swells that particular domain, thus changing its size, and sometimes the swelling is enough to cause a morphological transition.[92−94] This method was employed here; a **PS**−**PLA** block copolymer of lamellar morphology was blended with **PSOH**, such that the **PS** domains swelled, resulting in a cylindrical morphology (**B(40, 0.42)** in Table 2). This blend along with the block copolymers **SL(32, 0.28)**, **SL(58, 0.38)**, and **SL(92, 0.36)** in Table 2 were then used as precursors to nanoporous materials exhibiting pore sizes other than 22 nm. They were aligned through channel die processing and then subjected to the same degradation regimen. Through direct synthesis and blending we prepared a series of nanoporous **PS** monoliths containing pore diameters ranging from 15 to 45 nm (Figure 8). A subset of these and their pore diameters are given in Table 3. They are given the nomenclature **dSL(*X*,*Y*)** where **dSL** refers to a **PS**−**PLA** precursor with a total molecular weight (***X*** kg/mol**)** and f_{PLA} (***Y***) that has been degraded to yield nanoporous materials.

Nitrogen Adsorption. Adsorption techniques are typically employed to determine the surface area and pore size distributions of porous materials.[42,95−97] The surface area for three of the porous materials was calculated using the Brunauer−Emmett−Teller (BET) theory. The BET surface areas were in good agreement with those calculated using the pore diameters and spacings found from SAXS and assuming that the cylindrical pores run uninterrupted throughout the sample length (Table 3). This lends evidence to the fact that this system yields a well-ordered network composed of regularly sized pores. More evidence for the narrow pore size distributions of these nanoporous materials was found from a more detailed analysis of **dSL(37, 0.38)** in Table 3. The adsorption of nitrogen (at T

(91) Xia, Y.; Kim, E.; Whitesides, G. M. *Chem. Mater.* **1996**, *8*, 1558−1567.
(92) Kinning, D. J.; Thomas, E. L.; Fetters, L. J. *J. Chem. Phys.* **1989**, *90*, 5806−5825.
(93) Tanaka, H.; Hasegawa, H.; Hashimoto, T. *Macromolecules* **1991**, *24*, 240−251.
(94) Winey, K. I.; Thomas, E. L.; Fetters, L. J. *Macromolecules* **1992**, *25*, 422−428.
(95) Sing, K. S. W. *Adv. Colloid Interface Sci.* **1998**, *76/77*, 3−11.
(96) Øye, G.; Sjöblom, J.; Stöcker, M. *Adv. Colloid Interface Sci.* **2001**, *89/90*, 439−466.
(97) Kresge, C. T.; Leonowicz, M. E.; Roth, W. J.; Vartuli, J. C.; Beck, J. S. *Nature* **1992**, *359*, 710−712.

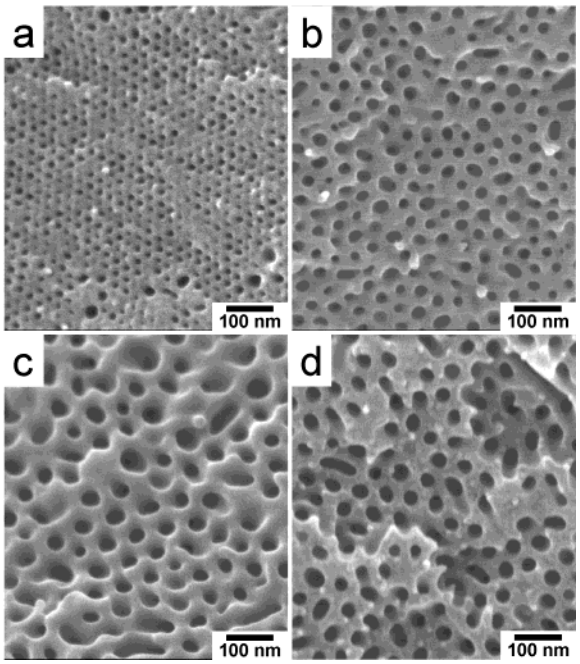

Figure 8. Scanning electron micrographs perpendicular to the cylinder axes for nanoporous materials: (a) **dSL(32, 0.28)** (D_{cyl} = 15 nm), (b) **dSL(58, 0.38)** (D_{cyl} = 31 nm), (c) **dSL(92, 0.36)** (D_{cyl} = 45 nm), and (d) **dSL(40, 0.42)** (D_{cyl} = 42 nm) in Table 3. The diameter of the cylinder, D_{cyl}, as determined by SAXS agrees well with the pore diameter found from SEM when accounting for the Pt-coating thickness.

Table 3. Characterization of Porous Materials

sample[a]	D_{cyl} (nm)[b]	calcd S.A. (m^2/g)[c]	BET S.A. (m^2/g)[d]	calcd SFE (J/g)[e]	$-\Delta H$ from DSC (J/g)[f]
dSL(32, 0.28)	15	96			
dSL(37, 0.38)	22	96	111	3.9	4.8
dSL(40, 0.42)[g]	42	65			
dSL(58, 0.38)	31	75	66	2.3	3.5
dSL(92, 0.36)	45	48	38	1.3	1.3

[a] **dSL(*X*,*Y*)** = degraded **PS**−**PLA** that originally had a total molecular weight (***X*** kg/mol) and f_{PLA} (***Y***). [b] Cylinder diameter determined from SAXS. [c] Calculated from the pore diameters and intercylinder spacings found from SAXS assuming that the cylindrical pores run uninterrupted throughout the monoliths. [d] Surface area determined through BET (see Experimental Section). [e] Surface free energy calculated from BET surface area and γ_{PS} = 35 mJ/m^2 at 100 °C.[100] [f] Change in enthalpy calculated from the area of the exotherm in the DSC. [g] Prepared from **B(40, 0.42)** in Table 2.

= 77 K) by this material exhibits a Type IV isotherm which is identified by a hysteresis loop between the adsorption and desorption branches, a signature of nanoporous materials (Figure 9).[42] The adsorption branch was used to determine nanopore size. For the case of **dSL(37, 0.38)**, a sharp increase in the uptake of the nitrogen adsorbate occurs at around $p/p^0 = 0.9$ which is indicative of a material containing pores with diameters around 20 nm. This isotherm of adsorption versus relative pressure was transformed to give a pore size distribution for **dSL(37, 0.38)** showing a very narrow pore size distribution centered around a diameter of 24 nm and a Barrett−Joyner−Halenda (BJH) calculated average pore diameter of 16 nm (Figure 9, inset). While the BJH calculation should provide a good measure of pore size since it is based on a cylindrical pore model, the actual value is generally higher.[42,98] Curvature effects (surface tension is dependent on curvature and thus

(98) Ahn, W. S.; Jhon, M. S.; Pak, H.; Chang, S. *J. Colloid Interface Sci.* **1972**, *38*, 605−608.

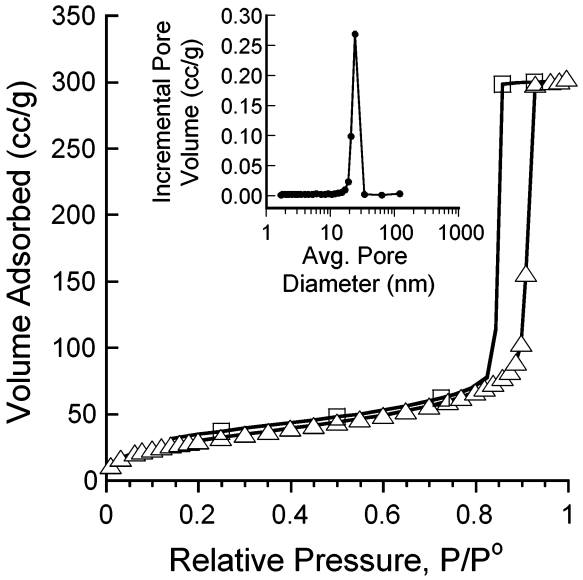

Figure 9. Adsorption of N_2 by **dSL(37, 0.38)** in Table 3 exhibits a Type IV isotherm characteristic of nanoporous materials (triangles = adsorption branch, squares = desorption branch). (Inset) Pore size distribution for this material centered around 24 nm.

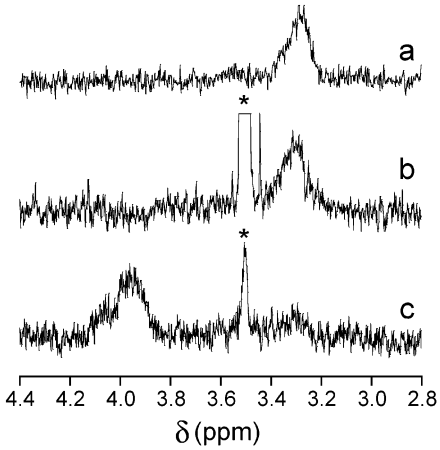

Figure 10. ^{1}H NMR spectra showing the methylene resonance for: (a) **PSOH(22)** in Table 1 (PS−CH_2−C**H_2**−OH) (b) **dSL(37, 0.38)** in Table 3 and (c) trifluoroester-functionalized porous material (PS−CH_2−C**H_2**−O(CO)CF_3); 81 ± 4% of the hydroxyl groups were converted. ∗ Denotes residual methanol in the samples.

deviates from bulk values in the voids) cause the pore size to be underestimated. Uncertainties in temperature (thermal leak to the surroundings can cause the temperature of the sample to be higher than expected) also result in the measured pore size being low with these errors being realized to a greater extent for larger pore sizes. Taking into account that the BJH pore diameter is probably low, its value is consistent with the SAXS-determined pore size of 22 nm for this material and is further evidence to the fact that this block copolymer-templated route to porous materials leads to materials with narrow nanopore size distributions.

End-Group Functionalization. In the synthesis of **PS**−**PLA**, the two chains are connected through an ethoxy group. Since the chains are incompatible, this group lies at the interface between the **PS** and **PLA** domains. Upon removal of the **PLA** fraction, the mild degradation chemistry should leave hydroxyl functionalities lining the walls of the pores. We estimate from the BET-determined surface area and **PSOH** molecular weight

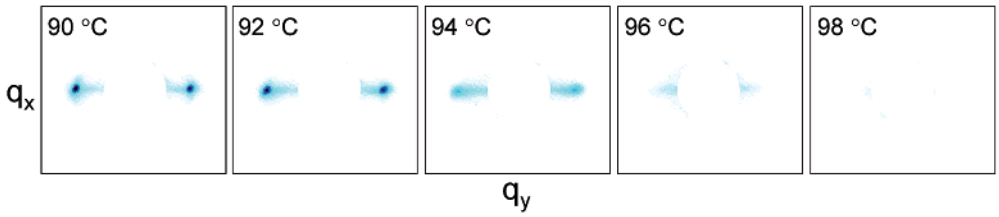

Figure 11. Temperature dependence of the 2-D SAXS pattern for **dSL(37, 0.38)** in Table 3 which was channel die-processed ($F_2 = 0.90$) before removal of the **PLA**. The white circle in the center of each pattern is blocking the beamstop position and some of the surrounding parasitic scattering.

that the areal density of functional groups on the pore wall would be 0.25/nm^2 for **dSL(37, 0.38)** if all the functional groups remain present at the surface. Evidence that the functionality remains after degradation was seen in the ^{1}H NMR spectrum of **dSL(37, 0.38)** in Table 3 (Figure 10b). The methylene resonance similar to that of **PSOH(22)** in Table 1 remains after degradation (Figure 10a). To determine whether the functionality is accessible and modifiable, the nanoporous monoliths were submerged in neat trifluoroacetic anhydride. The reaction of the hydroxyl groups with anhydride resulted in the formation of trifluoroacetate esters. To confirm that the reaction was indeed taking place in the pores and not upon dissolving it in $CDCl_3$ for ^{1}H NMR analysis, the piece was soaked in methanol to react with and remove the excess trifluoroacetic anhydride from the channels.[99] It was thoroughly dried in a vacuum oven at room temperature. The porous framework of the functionalized monolith was unharmed by the procedures as evidenced by 2-D SAXS analysis. A portion of the ester-functionalized monolith was then analyzed by IR showing a stretch at 1786 cm^{-1} which can be attributed to the carbonyl stretch of the trifluoroester; indicating that the reaction was occurring in the pores. Further corroboration of the reaction in the pores was provided by the ^{1}H NMR of the ester-functionalized monolith (Figure 10c). Upon transformation of the hydroxyl group to the trifluoroester, the methylene signal of the end group shifted from ~3.3 to ~4.0 ppm. The reaction was not complete but indicated that 81 ± 4% of hydroxyl groups reacted. This evidence supports the hypothesis that the end-group functionality for the most part lies on the surface of the pore walls with perhaps a minority of the groups buried in the matrix. Changing the functionality may have great importance in using these frameworks as scaffolds for nanomaterial synthesis in terms of what substances can be drawn into the voids.

Thermal Stability and Surface Energy. The thermal stability of the porous materials will have consequences as to what procedures and ultimately in what applications it can be employed. The thermal stability for **dSL(37, 0.38)** in Table 3 was analyzed by 2-D SAXS with its temperature dependence given in Figure 11. The principal reflections are no longer observable above 94 °C, indicating that the ordered array of nanopores no longer exists at these elevated temperatures. To further characterize its stability, the material was analyzed by differential scanning calorimetry (DSC). Upon heating the sample at 10 °C/min, an exotherm was observed (Figure 12b). After the sample was cooled, the temperature was increased again, and a glass-transition was observed (Figure 12c). As expected, this transition occurred at the same position as the corresponding **PSOH** (Figure 12a). The exotherm was also

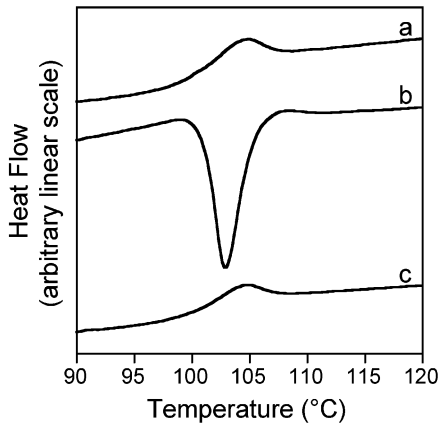

Figure 12. DSC at 10 °C/min of (a) **PSOH(22)** in Table 1 showing its glass-transition. (b) **dSL(37, 0.38)** in Table 3 showing an exotherm upon heating through the glass-transition of **PS**. (c) **dSL(37, 0.38)** on second heating after cooling to 20 °C showing the glass-transition for the sample being identical to the corresponding **PSOH**.

located at this temperature. We propose that this is due to the collapsing of the structure in which surface area is being eliminated, and hence, the excess surface energy is being released. This proposal is in agreement with the observation from SAXS. The area of the exotherm observed by DSC corresponds to a change in enthalpy (ΔH), excluding the area associated with the glass-transition, which can be related to the surface free energy in the following way:

$$\Delta H = T\Delta S + \gamma\Delta A \qquad (10)$$

where γ is the surface free energy and ΔA is the change in area with no change in pressure occurring in the process. From this, it is expected that the amount of heat released upon collapse of the framework would be correlated to the change in surface area. This is what is observed from the DSC measurements.

While there is no easy way to account for the change in entropy (ΔS) upon collapsing the structure, the change should be positive since the chains have more freedom above the glass-transition temperature and the chain ends will no longer be forced to be on the pore wall surfaces. This effect would lessen the magnitude of ΔH upon collapse. The value of $\gamma\Delta A$ was calculated for each system using the surface area determined from BET as the change in area (the surface area of the outer surface being negligible compared to the internal surface area) and γ as the surface free energy of **PS** (γ_{PS}) at 100 °C, 35 mJ/m^2.[100] While this value of surface free energy may not be directly applicable to our system due to the presence of hydroxyl groups at the surface of the voids for these systems, poly(vinyl alcohol) has a surface free energy value similar to that of **PS**.

(99) The methanol may be hydroxylating the trifluoroacetate ester groups, distorting the calculation of end-group accessibility.

(100) Wu, S. *J. Phys. Chem.* **1970**, *74*, 632−638.

As such, the use of γ_{PS} as the value for our system is not unreasonable. The calculated values for $\gamma\Delta A$ are relatively close to the measured ΔH's for all systems (Table 3). While the measurement and calculation are not quantitative, the trend of surface area to observed ΔH is followed, giving credence to the hypothesis.[101]

Summary

We have demonstrated the preparation of polymeric monoliths exhibiting a hexagonally packed array of nanoscopic pores from **PS−PLA** block copolymer precursors. The self-assembly of block copolymers into ordered morphologies was exploited along with the ability to macroscopically align them either through reciprocating shear or shear flow. The degradability of the minor component, **PLA**, along with the mild degradation chemistry allowed for the formation of a voided structure without disturbing the remaining porous **PS** framework as evidenced by both SAXS and SEM. We demonstrated that an anisotropic pathway throughout the porous material exists. This system offers much flexibility as precursors to porous materials in that the pore sizes and spacing can be modified through synthesis or blending. This **PS−PLA** templated route to nanoporous materials also results in the desirable characteristic of narrow pore size distributions. Furthermore, the degradation chemistry results in hydroxyl functionalization within the channels of the porous materials. This functionality is both accessible and tunable providing "reactive handles" with which the pore functionality could be modified. The controllability of the block copolymer synthesis, the ability to modify the pore dimensions, the capability of making bulk materials by aligning the self-assembled morphologies through shear, along with the capacity to change the chemical environment of the channels allow these materials to be tailored to a variety of applications.

Acknowledgment. This work was supported by the National Science Foundation (DMR-0094144) and the David and Lucille Packard Foundation. We thank Charles J. Taylor for help with the SEM imaging, Mohammed Al-Daous for help with nitrogen adsorption measurements, and Yunbing Wang with the large-scale synthesis of **PS−PLA**. Andrew S. Zalusky thanks the Department of Chemistry at the University of Minnesota for financial support through a departmental fellowship. Roberto Olayo-Valles acknowledges support from a CONACYT/Fullbright-Garcia Robles Grant 119158.

Supporting Information Available: Figures S1 and S2 (PDF). This material is available free of charge via the Internet at http://pubs.acs.org.

JA0278584

(101) While we suspect that the surface energy of the trifluoroester-functionalized porous material is lower than the hydroxyl-functionalized monoliths, no statistically different response was observed by DSC.

(102) Höcker, H.; Blake, G. J.; Flory, P. J. *Trans. Faraday Soc.* **1971**, *67*, 2251−2257.
(103) Witzke, D. R.; Narayan, R.; Kolstad, J. J. *Macromolecules* **1997**, *30*, 7075−7085.